



HAL
open science

A 3D analysis of the onset of slip activity in relation to the degree of micro-texture in Ti–6Al–4V

S. Hémery, Azdine Nait- Ali, M. Gueguen, J. Wendorf, A.T. Polonsky, M.P. Echlin, J.C. Stinville, T.M. Pollock, P. Villechaise

► To cite this version:

S. Hémery, Azdine Nait- Ali, M. Gueguen, J. Wendorf, A.T. Polonsky, et al.. A 3D analysis of the onset of slip activity in relation to the degree of micro-texture in Ti–6Al–4V. *Acta Materialia*, 2019, 181, pp.36-48. 10.1016/j.actamat.2019.09.028 . hal-02316551

HAL Id: hal-02316551

<https://hal.science/hal-02316551>

Submitted on 20 Jul 2022

HAL is a multi-disciplinary open access archive for the deposit and dissemination of scientific research documents, whether they are published or not. The documents may come from teaching and research institutions in France or abroad, or from public or private research centers.

L'archive ouverte pluridisciplinaire **HAL**, est destinée au dépôt et à la diffusion de documents scientifiques de niveau recherche, publiés ou non, émanant des établissements d'enseignement et de recherche français ou étrangers, des laboratoires publics ou privés.



Distributed under a Creative Commons Attribution - NonCommercial 4.0 International License

A 3D analysis of the onset of slip activity in relation to the degree of micro-texture in Ti-6Al-4V

S. Hémerly^a, A. Naït-Ali^a, M. Guéguen^a, J. Wendorf^b, A.T. Polonsky^b, M.P. Echlin^b, J.C. Stinville^b, T.M. Pollock^b, P. Villechaise^a

^a Institut Pprime, ISAE-ENSMA, Université de Poitiers, CNRS UPR 3346, 86962 Chasseneuil Cedex, France.

^b University of California Santa Barbara, Santa Barbara, USA.

Abstract

The mechanical properties of titanium alloys result from their complex multi-scale microstructural features, including micron scale precipitates and millimeter scale microtextured regions (MTRs). While previous investigations have revealed that the presence of mm-scale MTRs can degrade mechanical properties, particularly fatigue, the accompanying strain localization processes that operate at the microscale within the α grains in MTRs are not well understood. The present work is a mechanistic investigation of MTRs using crystal plasticity simulations of mm³-scale experimentally captured and synthetically generated 3D microstructure datasets. The explicit modeling of both the α grains and MTRs in Ti-6Al-4V enables assessment of the effect microtexture and local structure variations within the MTR on overall deformation behavior and the onset of plastic slip in MTRs. The presence of MTRs with a dominant [0001] orientation results in both stress and plastic strain hotspots during the early stages of straining. Crystal plasticity predictions are compared to previous digital image correlation studies on early strain localization. The influence of MTRs on the local stress and strain fields is discussed with regard to the monotonic tension, fatigue and dwell-fatigue behavior of titanium alloys.

Keywords: Titanium alloys, microtexture, crystal plasticity, 3D EBSD, macrozones

1. Introduction

The mechanical properties of α/β titanium alloys can be tailored for a wide range of applications depending on the processing pathway. Typically, processing routes tune microstructural features such as the type of microstructure, the size and morphology of precipitates, and texture [1]. Fatigue performance is critical for aero-engine applications since the loading is cyclic in nature and is highly sensitive to the microstructure including the size and shape of alpha precipitates and the volume fraction of primary alpha phase [2].

For example, poor resistance to fatigue crack nucleation was previously reported for fully lamellar microstructures. A long effective slip length results from the beta layers that separate the alpha platelets and are soft barriers to dislocations glide [3]. Conversely, equiaxed or bi-modal microstructures often exhibit a higher resistance to crack nucleation due to a reduced slip length that is approximately equal to the α grain size. However, recent studies highlighted that the presence of micro-textured regions (MTRs), which result from the α/β processing step could have a major effect on the effective slip length [4,5]. These band-like regions with sharp textures can contain α grains with preferred orientations that favor the occurrence of long range slip localization [6,7]. Indeed, the occurrence of slip transfer across low angle grain boundaries in Ti-6Al-4V has been reported recently [8]. The consequential increase in effective slip length, which is set by the size of the MTRs, is expected to have a detrimental effect on the fatigue performance [2].

Dwell-fatigue crack growth is observed to accelerate in MTRs with a dominant [0001] orientation [9], which is believed to significantly contribute to the cold dwell fatigue life debit that occurs if a load hold

at maximum stress is introduced during cycling [10]. The minimal retardation of small fatigue crack growth in these MTRs was also considered in order to understand why a given crack would become the dominant crack, causing specimen failure [11] as well as fatigue life discrepancies [12]. Cracks have also been shown to preferentially nucleate within MTRs with a dominant [0001] orientation during fatigue [13–15] and dwell-fatigue [16] loadings. In order to obtain a mechanistic understanding, simulations of the deformation behavior of idealized microtextured polycrystals successfully captured long range strain localization behavior at the mesoscale [7]. Following the work of Bridier et al. [14], a mechanical effect of MTRs on the onset of slip activity was also observed, based on slip trace analysis [17] and simulation of the stress and strain fields within an anisotropic elasticity framework [18]. Elastic-visco-plastic modeling using experimentally collected 3D microstructural data for the investigation of the mechanical effects related to the presence of MTRs has not been reported yet. This is of critical concern because the generation of synthetic or statistically equivalent microstructures, which are often based on distributions extracted from experimental data, may not reproduce critical features driving deformation and damage. For instance, prior simulation works highlighted a significant effect of grain shapes on the mechanical fields [19].

Two major technical obstacles have prevented multi-scale simulations of deformation of titanium alloys. First, the collection and reconstruction of large mm³-scaled 3D microstructural volumes necessary to capture both the MTRs and an accurate description of the microscale microstructural elements, including the primary α grains, is a technical challenge. The recent development of 3D data collection techniques including mechanical serial sectioning [20], plasma focused ion beam [21], high energy X-ray diffraction microscopy [22] and femtosecond laser ablation [23] now permits the collection of datasets large enough for the analysis of the effects of MTRs on mechanical properties. The second challenge is the ability to simulate the deformation behavior of these large 3D datasets within a crystal plasticity framework. For instance, classical finite element-based crystal plasticity models, which are suitable for the grain scale mechanistic understanding of deformation [24–26], are limited in terms of the number of voxels. As an alternative, cellular automata have been successfully applied to simulate the deformation behavior of titanium alloys considering a large number of grains with an idealized microstructure [27]. The recent development of Fast-Fourier Transforms (FFT)-based crystal plasticity simulations have overcome these computational limitations [28,29].

In the present article, we report an investigation of the effect of MTRs on the early slip activity using FFT based crystal plasticity simulations on experimental 3D microstructures gathered using TriBeam 3D EBSD. This reconstruction technique has the advantage of capturing both the crystallographic orientation and the grain morphologies and arrangements in 3D for volumes consistent with the study of MTRs. In this study the simulated deformation behavior was compared at the macroscale as well as at the grain level with experimental measurements captured using high-resolution digital image correlation reported in detail in a prior study on the same experimental sample [6]. Synthetic datasets with different degrees of microtexture were then generated to investigate the intrinsic effect of MTRs on mechanical properties.

2. Material and experiments

2.1 Material

A Ti-6Al-4V alloy subjected to deformation processing and subsequent annealing in the α / β phase field developed a spectrum of relatively fine-scale α / β microstructures. The material used in this study was homogenized in the beta phase field, cooled, and then rolled into plate at a temperature just below the α / β transus. Subsequently, the plate was heat treated at 926°C for 4 h and cooled to room temperature at 0.3°C/minute to homogenize the residual strain present from the hot working steps. The resulting microstructure possessed an average α grain size of about 10 μm and the beta phase fraction is approximately 8%. The microstructure, the composition and the texture of the material is outlined in more detail elsewhere [6,7], and examined in 3D in the present study.

A tensile test was performed with a 10^{-4} s^{-1} strain rate in order to compare the simulations with experimental macroscopic mechanical response. The gage length of this specimen is 10 mm, its width is 2 mm and its thickness is 1 mm.

2.2 Microstructure reconstruction

Three-dimensional characterization was performed by TriBeam, an in-situ FIB-SEM microscope femtosecond laser-based mesoscale tomography technique [23]. The TriBeam tomography experiment performed on the Ti-6Al-4V alloy in this article involved femtosecond laser sectioning at a shallow glancing angle, followed by a 65 nA FIB cleaning step and collection of both secondary electron images and electron backscatter diffraction (EBSD) maps within each slice. An in-plane EBSD imaging resolution of $1.5 \mu\text{m}$ was employed, using a 4x4 binning mode on the EBSD detector. The sectioning resolution, set by stage movements into the laser beam, was also set at $1.5 \mu\text{m}$, resulting in cubic voxels with a side length of $1.5 \mu\text{m}$. Imaging was performed using a 30 kV electron beam. The 3D reconstruction was performed using DREAM.3D [30]. Briefly, the reconstruction process required a registration (slice alignment step) and a 2° misorientation tolerance for segmentation to define the grains boundaries. Only the α phase was considered due to the small size and the low fraction of retained β phase at room temperature. Grain averaged Euler angles were used in the following.

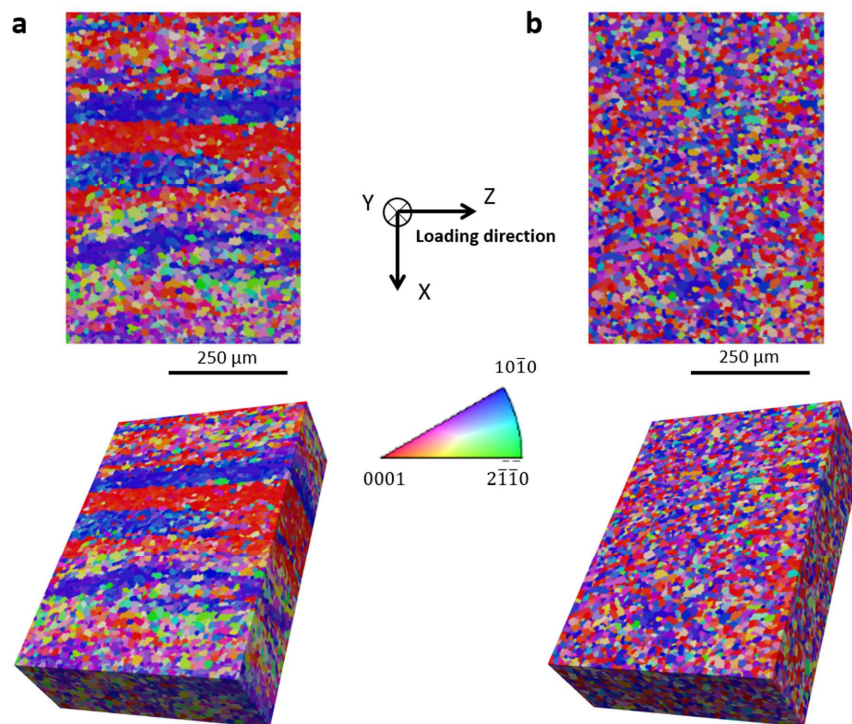


Figure 1 a. Reconstructed microstructure with inverse pole figure colors indicating the crystallographic orientation relative to the Z direction, and overall dataset size of $198 \mu\text{m} \times 715.5 \mu\text{m} \times 508.5 \mu\text{m}$, b. Synthetically generated microstructure with inverse pole figure colors indicating the crystallographic orientation relative to the Z direction. The experimentally collected and synthetic microstructures with the same macrotexture contain different degrees of microtexture.

The dimensions of the 3D gathered dataset are $198 \mu\text{m} \times 715.5 \mu\text{m} \times 508.5 \mu\text{m}$. It contains about 21 million voxels distributed over more than 57000 α grains with experimentally captured morphologies and crystallographic orientations. The crystal orientations relative to the Z-axis are plotted on the surface of the reconstructed 3D dataset in figure 1a. Several MTRs with dominant $[0001]$, $[10\bar{1}0]$ or mixed orientations are present. These regions run lengthwise in the Y and Z directions. The macrotexture of the dataset is presented in figure 2a using an orientation density function plotted on $[0001]$ and $[10\bar{1}0]$ pole figures.

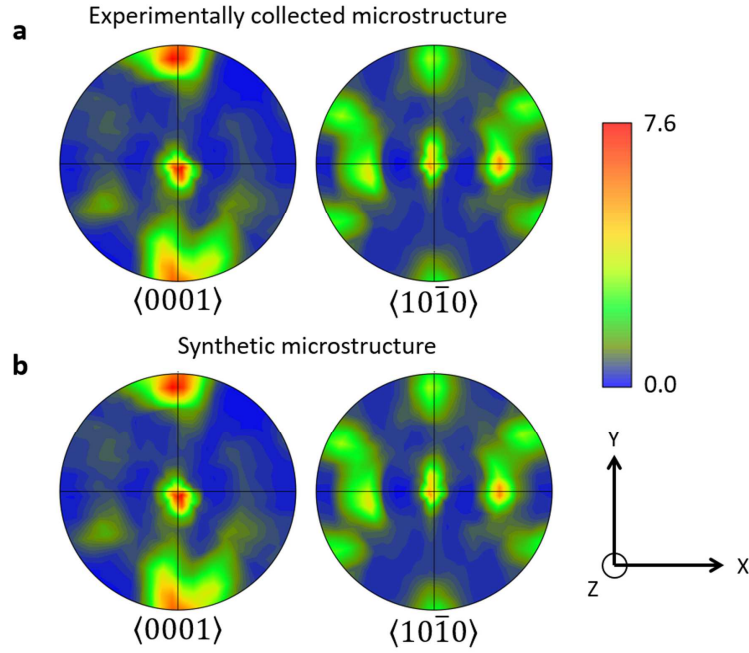


Figure 2 Orientation density function plotted on pole figures showing similar macrottextures for the a. experimentally gathered 3D dataset and the b. synthetic microstructure.

The 3D dataset was collected from the identical tensile specimen tested in a prior study [6]. In this previous work, the specimen was tested in tension at low strains in order to analyze the early slip activity using digital image correlation in the scanning electron microscope (SEM). This procedure has the advantage of using strain fields to validate the agreement between the experimental and simulated deformation behaviors. 3D information was gathered from the region below the surface where DIC strain measurements were collected, and showed no significant changes in the reconstructed microstructure due to the imposed strain. This is not surprising given that the sample was only loaded to the onset of yield, where the lattice rotations induced by the deformation are low [31].

2.3 Synthetic microstructure generation

The effects of MTRs on the global and local behaviors were isolated by comparison with a carefully designed synthetic dataset. The macrottexture was kept nominally constant while MTRs were removed, in order to prevent any effect of the texture at the dataset scale. An approach that is outlined in more detail elsewhere for use with 2D data was employed [18]. It consists of reassigning the crystallographic orientation of a given grain in a dataset to a different random grain of the dataset. The crystalline orientation relative to the Z-axis is plotted on the surface of the synthetic 3D dataset in figure 1b after complete redistribution of the crystallographic orientations. MTRs, such as visible in figure 1a, have successfully been removed. The macrottexture of the synthetic dataset is presented in figure 2b using an orientation density function plotted on $[0001]$ and $[10\bar{1}0]$ pole figures. The macrottexture of the experimentally gathered 3D dataset is preserved in the synthetic dataset, as shown in the pole figures. This synthetic dataset is used to investigate the deformation behavior of a microstructural region with a similar macrottexture as well as grain size and morphology distributions but different degrees of microtexture.

2.4 Simulation methods

The onset of slip activity was studied using FFT-based crystal plasticity simulations due to its calculation efficiency and its ability to operate directly on voxelized data, such as gathered by the TriBeam tomography approach. The FoxTrot in-house code was employed [32]. In comparison to the finite element method, periodic boundary conditions have to be applied and no meshing is required. The cubic voxel discretization leads to a poor description of the fields near the boundaries, but this study does not focus on the boundary effects of deformation. In the present study, the formulation of the elastic-visco-plastic model

is taken from [28]. This straightforward model involves a limited number of material parameters that can be easily identified from experiments or are reported in the literature. For more details about the model and the simulation procedures, the reader may refer to [28].

Using an Euler explicit discretization scheme and Hooke's law, the expression, in small strains, of the Cauchy stress tensor in material point \mathbf{x} at $t + \Delta t$ is given by equation (1).

$$\boldsymbol{\sigma}(\mathbf{x}) = \mathbf{C}(\mathbf{x}):(\boldsymbol{\varepsilon}(\mathbf{x}) - \boldsymbol{\varepsilon}^{P,t}(\mathbf{x}) - \dot{\boldsymbol{\varepsilon}}^P(\mathbf{x}, \boldsymbol{\sigma})\Delta t) \quad (1)$$

With $\boldsymbol{\sigma}(\mathbf{x})$ the Cauchy stress tensor at point \mathbf{x} , $\mathbf{C}(\mathbf{x})$ the elastic stiffness tensor, $\boldsymbol{\varepsilon}(\mathbf{x})$ the total strain tensor and $\boldsymbol{\varepsilon}^{P,t}(\mathbf{x})$ the plastic strain tensor. $\dot{\boldsymbol{\varepsilon}}^P(\mathbf{x})$ is calculated using equation (2):

$$\dot{\boldsymbol{\varepsilon}}^P(\mathbf{x}) = \sum_{S=1}^N \mathbf{m}^S(\mathbf{x})\dot{\gamma}^S(\mathbf{x}) \quad (2)$$

With $\mathbf{m}^S(\mathbf{x})$ the Schmid tensor of slip system S and $\dot{\gamma}^S(\mathbf{x})$ the shear strain rate on slip system S . The plastic shear rate is computed using equation (3).

$$\dot{\gamma}^S(\mathbf{x}) = \dot{\gamma}_0 \left(\frac{|\mathbf{m}^S(\mathbf{x}):\boldsymbol{\sigma}(\mathbf{x})|}{\tau_0^S} \right)^n \text{sgn}(\mathbf{m}^S(\mathbf{x}):\boldsymbol{\sigma}(\mathbf{x})) \quad (3)$$

With $\dot{\gamma}_0$ the reference plastic shear rate, τ_0^S the critical resolved shear stress for slip system S and n the inverse of the strain rate sensitivity. For simplicity purposes, the critical resolved shear stress is assumed to be constant throughout the simulation. This hypothesis is consistent with the low hardening rates in titanium alloys [25,33]. Furthermore, previous studies reported a limited influence on the behavior at low strain values [7].

Elastic constants have been taken from the pioneering work of Fisher and Renken on pure titanium [34]. Recent investigations revealed a good agreement with experimental data on Ti-7%Al [35]. Basal, prismatic and pyramidal slip systems are considered in the present simulations. Critical resolved shear stress values for basal and prismatic slip have been taken from Ti-6Al-4V with a similar α grain size [36] as it is known to be a significantly influential parameter [37]. The critical resolved shear stress for $\langle\mathbf{c}+\mathbf{a}\rangle$ pyramidal slip was calculated using the basal to pyramidal critical resolved shear stress ratio of 1.7 reported in [7]. The value of n , which is related to the strain rate sensitivity, was taken from [38,39]. A summary of the parameters used for the calculations and the associated values are indicated in table 1.

Parameter	C11	C12	C13	C33	C44	τ_0^{Basal}	$\tau_0^{Prismatic}$	$\tau_0^{Pyramidal}$	n	$\dot{\gamma}_0$
Value	162.4 GPa	92.0 GPa	69.0 GPa	180.7 GPa	46.7 GPa	338 MPa	352 MPa	700 MPa	50	10^{-7} s^{-1}
Reference	[32]	[32]	[32]	[32]	[32]	[34]	[34]	[7]	[36,37]	

Table 1 Material parameters used for the elastic-visco-plastic simulations

In order to reproduce the kinematic boundary conditions, an additional layer with infinite compliance was added on the free surface of the dataset. A displacement along the Z direction was applied to simulate tensile loading at a strain rate of 10^{-4} s^{-1} .

3. Results

3.1 TriBeam 3D experimental microstructure

The engineering stress – engineering strain curve obtained from the simulated tensile loading is shown in figure 3 for the TriBeam-generated microstructure. The Young's modulus is 116 GPa, which is in very good agreement with the experimental value reported in [6] for the same alloy with similar microstructure. The 0.2 % plastic strain offset is predicted to be 950 MPa. **The experimentally gathered stress – strain curve is presented in figure 3. Very similar behaviors are obtained both in the elastic and plastic regimes. The 0.2 % plastic strain offset is reached at 925 MPa. The difference between the simulated**

and the experimental values are less than 3%. A good agreement between the simulated and experimental responses is thus observed.

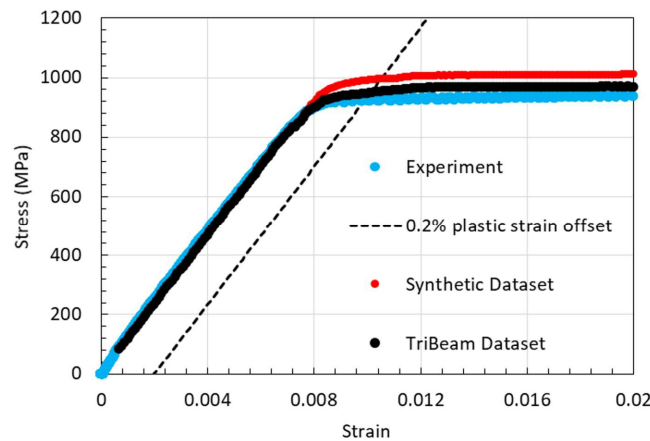


Figure 3 Engineering stress –strain curves of the experimentally collected and synthetic microstructures showing the tensile behavior. Significant differences depending on the degree of microtexture in the tested microstructural volume are observed. The experimental stress – strain curve obtained at a similar strain rate is also presented and reveals a good agreement between simulated and experimental behaviors.

The similarities in macroscopic responses are insufficient to demonstrate a proper reproduction of the grain scale deformation behavior. Therefore, experimental and simulated grain scale mechanical fields were compared. The strain field on the surface of the region reconstructed using 3D EBSD was experimentally characterized using DIC while loaded in tension. For further details, the reader is referred to a prior study [6]. As strain localization is not captured using classical crystal plasticity simulations, only locations of plastic strain hotspots were compared. The plastic strain field along the loading direction extracted from the crystal plasticity simulations is shown in Figure 4a at an applied stress of 822 MPa. The associated total strain is 0.71%. The strain field along the loading direction captured with DIC, which only accounts for plastic strain, is presented in figure 4b and 4c for total strains of 0.65 % and 0.71%. Plastic strain hotspots on the surface of the TriBeam dataset are indicated with dashed boxes and the corresponding locations are reported on the DIC strain field. The associated crystallographic orientation maps are shown in figure 4d and 4e. A careful comparison of both orientation maps reveals some differences, which result from difficulties in experimentally capturing the near surface microstructure in the early stages of the ablation process using TriBeam tomography (typically a few μm). As a consequence, a perfect correspondence between simulated and experimental fields is not expected. For instance, no slip activity is experimentally observed in the grain indicated by the green arrow in figure 4f while it is predicted by the simulations. In spite of these limited differences, the high strain in grains indicated by red arrows or in grain sets are correctly predicted with simulations. The comparison of experimentally collected and simulated strain fields thus reveals that the present simulations provide a very realistic mechanical response at both the grain and MTR scales.

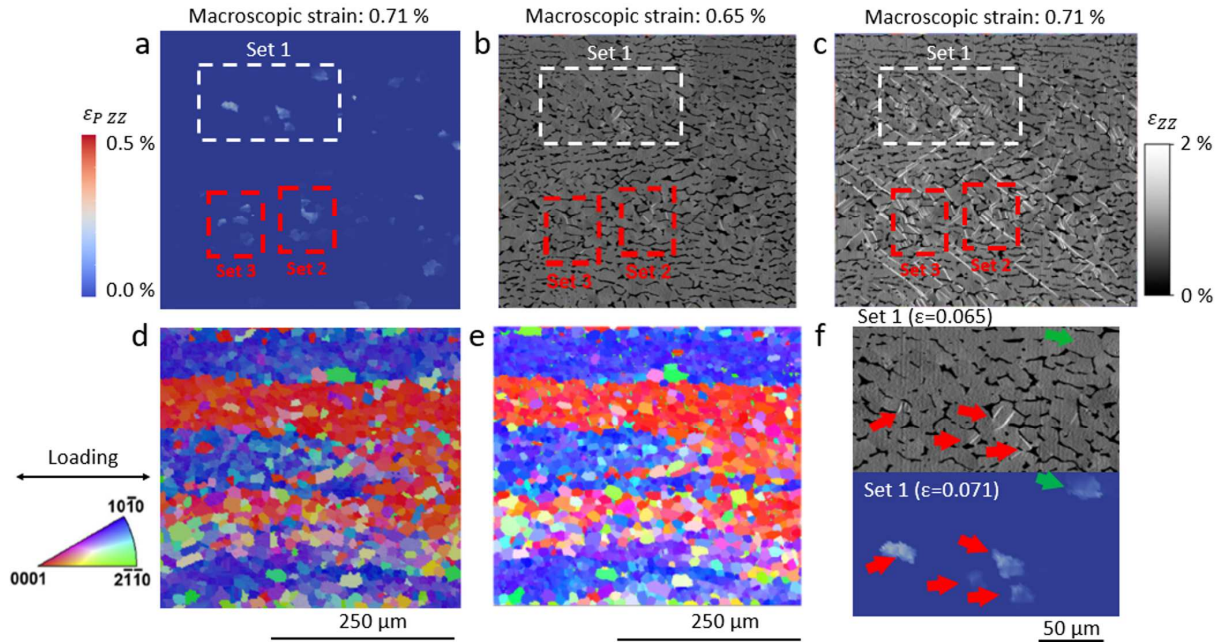


Figure 4 a. The ϵ_{PZZ} field extracted from simulations for a total strain of 0.71%, b. and c. the ϵ_{ZZ} strain fields obtained using high resolution digital image correlation for total strains of 0.65% and 0.71%, d. and e. crystallographic orientation maps along the loading direction on the surface of the Tribeam dataset and on the surface of the specimen, f. magnifications of the Set 1 regions shown in figure 4a. and 4b. The strain fields along the loading direction show a very good agreement and reproduction of experimental fields.

3.2 TriBeam 3D microstructure: elastic regime

The magnitude of σ_{ZZ} , which denotes the ZZ component of the stress tensor, at applied stress of 746 MPa is shown in figure 4b for the microstructure displayed on the inverse pole figure map along the loading axis in figure 5a. The average total strain is 6.4×10^{-3} with an average plastic strain lower than 10^{-5} . Hence, this step is associated with the elastic regime. Grains with a $[0001]$ direction (i.e. the c -axis of the hexagonal close packed lattice) well-aligned with the loading direction (i.e. the Z axis) display high σ_{ZZ} values as observed in Figure 5b. This observation conforms to expectations since the $[0001]$ direction is the stiffest direction of the hexagonal close packed lattice. The high density of such orientations in MTRs with a dominant $[0001]$ orientation lead to a high stress in these regions.

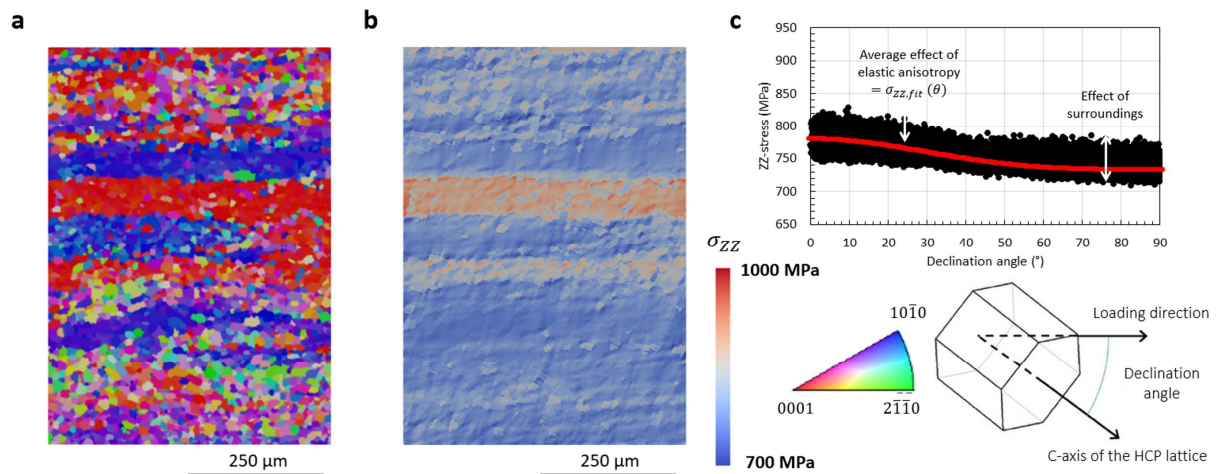


Figure 5 a. Inverse pole figure map of the crystalline orientation relative to the loading direction of the surface of the 3D TriBeam microstructure, b. the corresponding magnitude of σ_{ZZ} for an applied stress of 746 MPa, c. grain averaged magnitude of σ_{ZZ} plotted against the declination angle distinctly showing the average effect of elastic anisotropy (red line) and the effect of the surroundings (scatter around the red line).

The magnitude of σ_{ZZ} was averaged over each grain and is plotted in figure 5c as a function of the declination angle which is defined as the angle between the **c**-axis of the hexagonal close packed lattice and the loading direction. On average, higher σ_{ZZ} stresses are observed for declination angle close to 0° . Inversely, grains with declination angle close to 90° display lower σ_{ZZ} stresses. Similarly to the evolution of Young's modulus for α titanium, a progressive decrease of the average σ_{ZZ} stress is observed for declination angles from 0° to 90° . The average magnitude of σ_{ZZ} as a function of the declination angle, is obtained using equation (4).

$$\frac{1}{\overline{\sigma_{ZZ}(\theta)}} = C + B(\cos \theta)^2 + A(\cos \theta)^4 \quad (4)$$

With $\overline{\sigma_{ZZ}(\theta)}$ the average of σ_{ZZ} for a given value of the declination angle θ and A , B and C fitting constants. This equation originates from the expression of the Young's modulus as a function of the declination angle for a transversely isotropic elastic behavior. For further details about this equation, the reader may refer to [18]. The resulting curve, which reflects the average effect of the elastic anisotropy of the α phase, is plotted as a red line in figure 4c. On average, grains with the **c**-axis of the hexagonal close packed lattice closely aligned with the loading axis experience a higher σ_{ZZ} stress by about 50 MPa than grains with their **c**-axis misoriented by 90° from the loading axis. The associated order of magnitude, which is a few percent of the average of σ_{ZZ} , is consistent with both the correction of elastic anisotropy applied in [36] and the good description of slip activation reported in previous research considering a global stress state [40,41]. The scatter around the average value given by equation (4) for a given θ angle indicates the effect of the surroundings on the stress experienced by a given α grain. The term 'surroundings' used throughout this article includes microstructural features at different length-scales such as the direct neighbors for which a short-range mechanical effect can be expected (typically $< \alpha$ grain size), but also higher length-scale structures that may have long range mechanical effects (typically $> \alpha$ grain size). The scatter for a given θ angle does not appear as sensitive to the declination angle and is approximately ± 50 MPa. Interestingly, this is the same order of magnitude as the average effect of elastic anisotropy obtained using equation (4).

3.3 TriBeam 3D microstructure: early slip activity

The magnitude of σ_{ZZ} at applied stress of 852 MPa is shown in figure 6b for the microstructure displayed in the inverse pole figure map in figure 6a. The average total strain is 7.5×10^{-3} with an average plastic strain of 2×10^{-4} . This loading step is thus within the early slip activity regime.

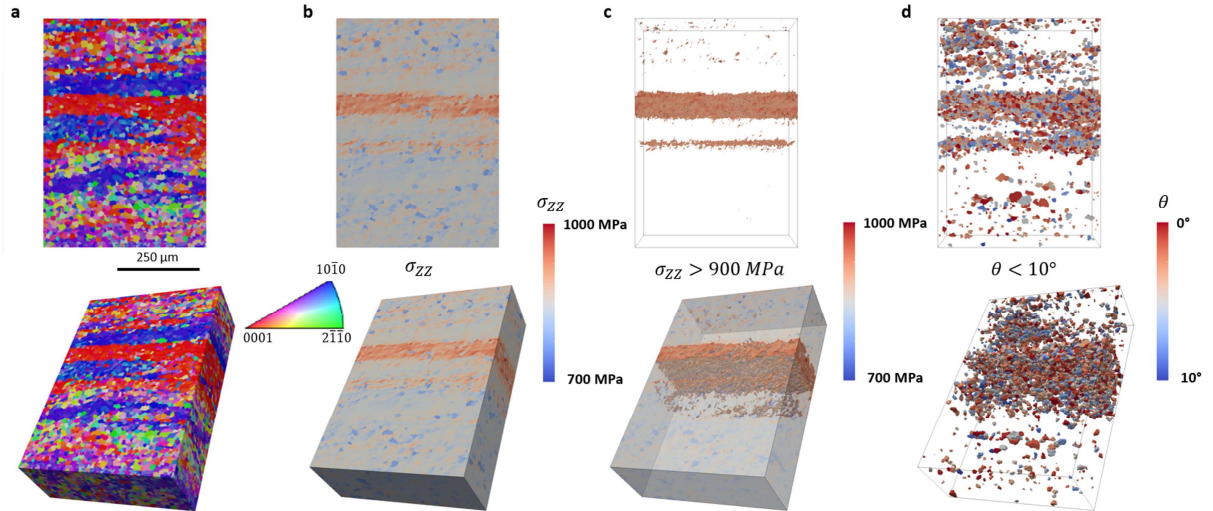


Figure 6 a. Inverse pole figure map of the crystalline orientation relative to the loading direction at the surface of the TriBeam 3D dataset, b. the corresponding magnitude of σ_{ZZ} for an applied stress of 852 MPa, c. voxels with a magnitude of σ_{ZZ} higher than 900 MPa and d. voxels with a declination angle lower than 10° (i.e. with a stiff orientation). The comparison of these maps highlights the effect of the MTRs on the presence and location of the stress hotspots.

Observations of the stress field map reveal stress heterogeneities in relation to the MTRs. In the elastic regime high stress magnitudes are located in the MTR with a dominant $[0001]$ orientation. Such behavior is expected owing to the high density of α grains with the c -axis of the hexagonal close packed lattice well aligned with the loading axis. In figure 6c, the voxels where σ_{ZZ} is lower than 900 MPa are hidden. This figure reveals that stress hotspots are mainly located in MTRs with a dominant $[0001]$ orientation. While these MTRs contain numerous grains with good alignment between the c -axis of the hexagonal close packed lattice and the loading axis, grains with similar orientations can be found elsewhere in the volume. In order to support this statement, a threshold on the value of the declination angle was used in order to hide all the grains where the declination angle exceeds 10° . According to this procedure, only grains with a stiff orientation are kept visible on figure 6d. Grains with the c -axis of the hexagonal close packed lattice well aligned with the loading axis are present both inside and outside MTRs with a dominant $[0001]$ orientation. The lack of stress hotspots outside of these MTRs reveals that the “grain neighborhood” is important to the development of hotspots and that local crystallographic orientation is insufficient to predict their location. MTRs with a dominant $[0001]$ orientation thus favor the presence of stress hotspots and are preferential locations for them.

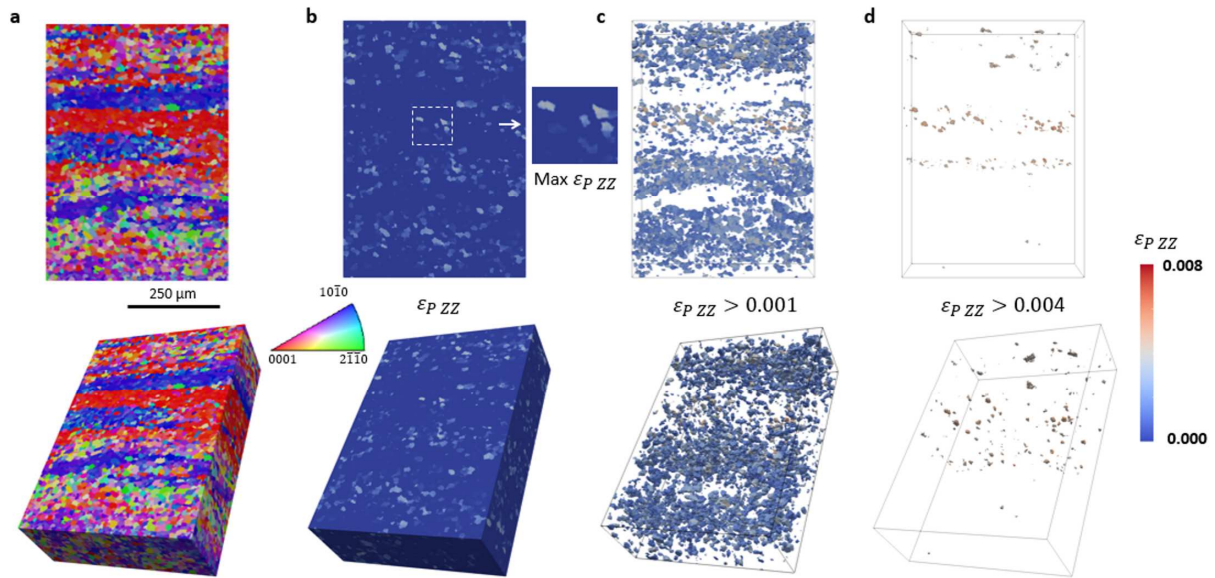


Figure 7 a. Inverse pole figure map of the crystalline orientation relative to the loading direction of the surface of the 3D TriBeam microstructure, b. the corresponding magnitude of $\epsilon_{P\ ZZ}$ for an applied stress of 852 MPa (the insert shows the highest values on the surface of the dataset), c. voxels with a magnitude of $\epsilon_{P\ ZZ}$ higher than 10^{-3} and d. voxels with a magnitude of $\epsilon_{P\ ZZ}$ higher than 4×10^{-3} . The comparison of these maps highlights an effect of MTRs on the presence and location of the plastic strain hotspots.

The ZZ component of the plastic strain tensor, which is denoted as $\epsilon_{P\ ZZ}$ in the following, at an applied stress of 852 MPa is plotted in figure 7b on the surface of the TriBeam 3D dataset. For convenience, the crystallographic orientation relative to the loading direction is reported in figure 7a. The maximum magnitude reached is 7.3×10^{-3} . At this loading step, the plastic strain field is highly heterogeneous. This reveals slip activation restricted to favorable microstructural configurations. Insights into the effect of MTRs on the plastic strain distribution are obtained considering figure 6c where the voxels with $\epsilon_{P\ ZZ}$ lower than 10^{-3} are hidden. The spatial distribution of the plastic strain at this loading step is significantly influenced by the presence of MTRs. In particular, MTRs with a dominant $[10\bar{1}0]$ orientation seem to resist plastic deformation. Such MTRs contain grains well oriented for prismatic slip, owing to a high Schmid factor for prismatic slip (≈ 0.42). Previous studies highlighted a higher applied stress required for the activation of prismatic slip than for the activation of basal slip [38]. The absence of plastic strain reveals that the stress in grains with a $[10\bar{1}0]$ direction well-aligned with the loading axis is insufficient to activate prismatic slip at the low strain values. The locations of plastic strain hotspots are represented in figure 7d, where voxels with

$\varepsilon_{p,ZZ}$ lower than 4×10^{-3} are hidden. Interestingly, plastic strain hotspots are mostly located in MTRs with a dominant $[0001]$ orientation. Again, the grains in which strain hotspots are located do not have good alignment between the c -axis of the hexagonal close packed lattice and the loading axis. Rather, they are well oriented for basal slip (i.e. very high Schmid factor for basal slip).

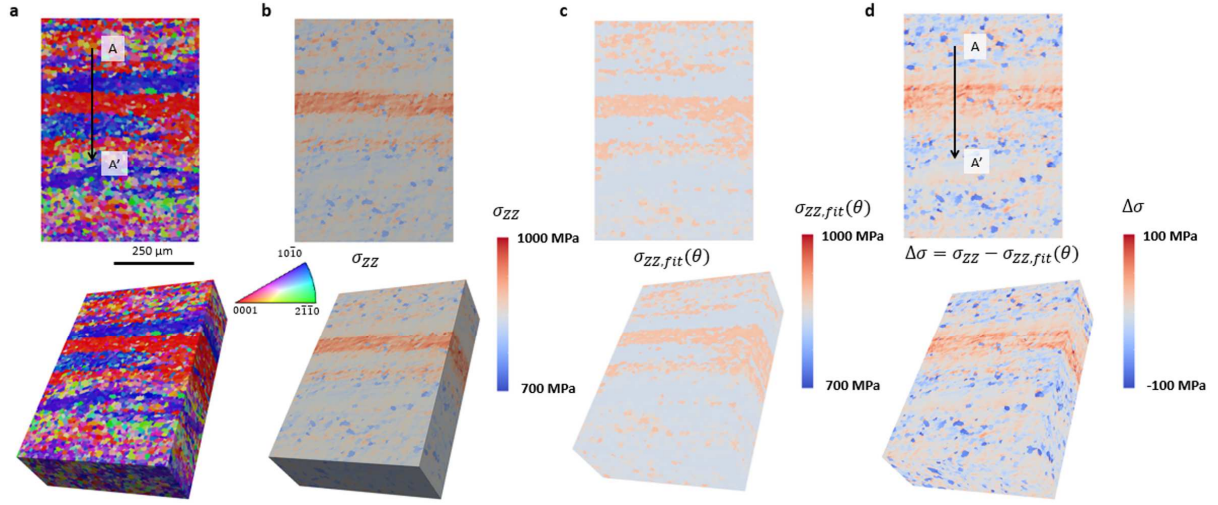


Figure 8 a. Inverse pole figure map of the crystalline orientation relative to the loading direction of the surface of the experimentally collected microstructure, b. magnitude of σ_{ZZ} of the surface of the TriBeam 3D microstructure for an applied stress of 850 MPa, c. the stress magnitude as calculated using equation (4) and reflecting the average effect of elastic anisotropy of α titanium and d. the difference between the fields plotted in figure 7b and figure 7c depicting the effect of the surroundings on the stress field.

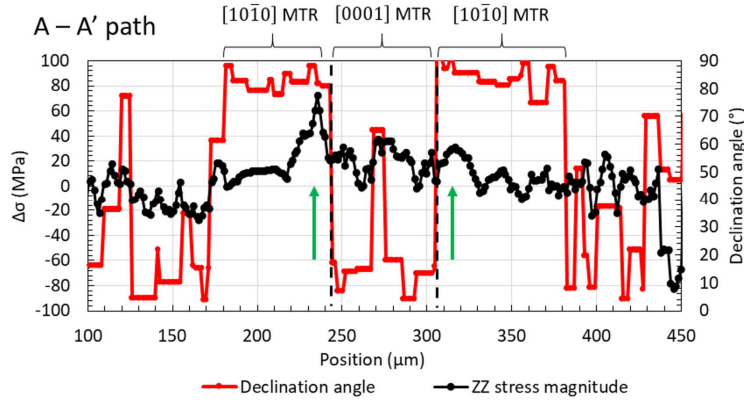


Figure 9 The stress profile along the line A – A' from Figure 8a. High stress is observed in the MTR with a dominant $[0001]$ orientation ($[0001]$ MTR), but also in MTRs with a dominant $[10\bar{1}0]$ orientation ($[10\bar{1}0]$ MTRs) nearby the interface with an $[0001]$ MTR (indicated by green arrows).

The previous analysis reveals that the stress field of a given voxel is influenced by the surroundings at different scales. This was investigated by de-correlation of the “average” effect of elastic anisotropy (including an averaged, or statistical, effect the surroundings) and the effect of the microstructural neighborhood, which are both included in the simulated stress field. The plot of σ_{ZZ} presented in figure 8b, will be decomposed into an average effect of elastic anisotropy and the scatter related to the effect of the surroundings.

Since the Young’s modulus of transversely isotropic materials can be expressed using the declination angle, a stress field representing the average effect of elastic anisotropy was calculated using the fit function presented in equation (4). The local magnitude of $\sigma_{ZZ,fit}(\theta)$, which accounts for a statistical effect of the elastic anisotropy instead of the real influence of the surroundings, was calculated using the value of the declination angle at each voxel. A linear correction was applied in order to obtain an average

stress of 852 MPa as opposed to 745 MPa, which corresponds to the applied stress at the step where the assessment of $\sigma_{ZZ,fit}(\theta)$ was carried out. The resulting stress field is shown in figure 8c. Finally, the difference between σ_{ZZ} , which includes the real influence of the surroundings, and $\sigma_{ZZ,fit}(\theta)$, which accounts for a statistical effect of the elastic anisotropy, is shown in figure 8d. The crystallographic orientation is given in figure 8a in order to facilitate the analysis of the relation with local crystallographic orientations and microtexture.

High stress magnitudes are present near plastically deforming grains due to strain incompatibilities across the interfaces. This may favor long range strain localization and connectivity of the strain path across the microstructure. Additionally, high stress magnitudes are present in the main MTR with a dominant [0001] orientation, confirming the effect of microtextured regions on the location of stress hotspots which was previously evidenced. However, this high stress region from the [0001] MTR also extends into the “soft” neighboring [10 $\bar{1}$ 0] MTR. While early strain localization does not occur in the [10 $\bar{1}$ 0] MTRs, these high stresses could play a significant role in early crack propagation.

This phenomenon is illustrated in the stress profile presented in figure 9 which was extracted from the field presented in figure 8d. Positive stress values are present in the MTR with a dominant [0001] orientation. Interestingly, this MTR contains a grain with a declination angle of 65°. This “soft” grain also experiences a high stress in spite of its singular orientation. This is expected to favor early slip activation in these regions. In addition, high stress values are observed in the neighboring MTRs with a dominant [10 $\bar{1}$ 0] orientation near their interface with the MTR with a dominant [0001] orientation. These features are indicated by green arrows in figure 9. The characteristic length of this effect is roughly 20 μm or a few α grain diameters. This feature suggests that the consideration of the direct neighborhood of a given grain is insufficient to accurately predict its stress or strain state.

3.4 Synthetic microstructure

The engineering stress - engineering strain curve obtained from the simulated 10^{-4} s^{-1} tensile test for the synthetic microstructure is reported in figure 3. The Young’s modulus is about 116 GPa and the 0.2 % proof stress is 994 MPa. Although no significant difference in the Young’s modulus exists between the TriBeam microstructure and the synthetic microstructure, the 0.2 % proof stress is decreased by 44 MPa (4.5 %) by the degree of microtexture present in the TriBeam microstructure.

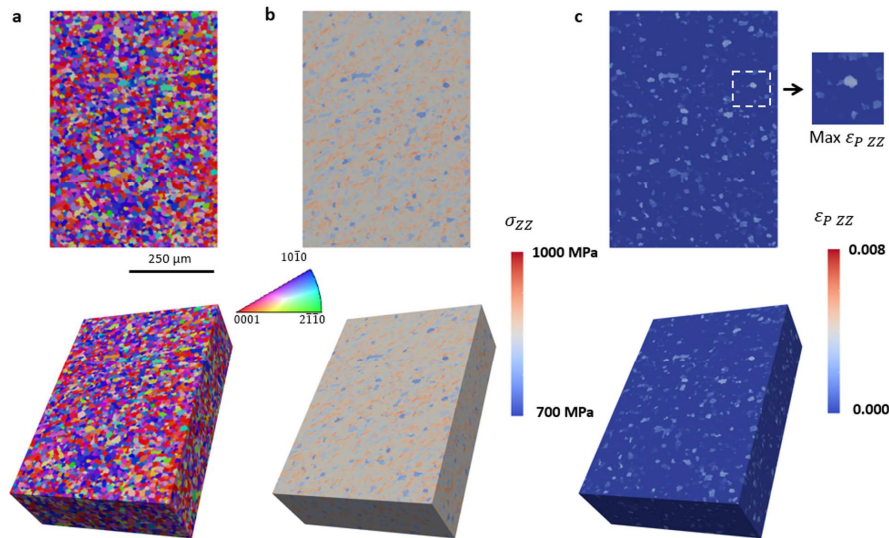


Figure 10 a. Inverse pole figure map of the crystalline orientations relative to the loading direction at the surface of the synthetic microstructure, b. the magnitude of σ_{ZZ} for an applied stress of 850 MPa, c. the magnitude of $\epsilon_{P\ ZZ}$ for an applied stress of 850 MPa (the insert shows the highest values on the surface of the dataset). More stress heterogeneities and higher plastic strain exist in the TriBeam 3D dataset despite a similar applied stress.

Maps of σ_{ZZ} and $\epsilon_{p,ZZ}$ in the synthetic microstructure are presented in figure 10 b and c for an applied stress of 850 MPa along with the crystallographic orientations relative to the loading axis in figure 10 a. A qualitative comparison of the fields presented in figures 6b and 7b for a similar applied stress reveals significant differences regarding the spatial distribution of the high and low stress magnitudes. At this loading step, the average total strain and the average plastic strain of the synthetic microstructure are 7.4×10^{-3} and 1.4×10^{-4} respectively. Higher average total strain and average plastic strain values are observed in the TriBeam dataset. $\epsilon_{p,ZZ}$ also locally reach higher values in the experimentally collected microstructure. The maximum plastic strain is 3.6×10^{-3} for the synthetic microstructure versus 7.3×10^{-3} for the TriBeam instantiated microstructure. These observations are in good agreement with the lower proof stress displayed by this microstructure. However, the stress fields in the TriBeam microstructure have both higher and lower magnitudes of σ_{ZZ} than the synthetic microstructure for a similar applied stress, showing that localization and heterogeneous loading are occurring.

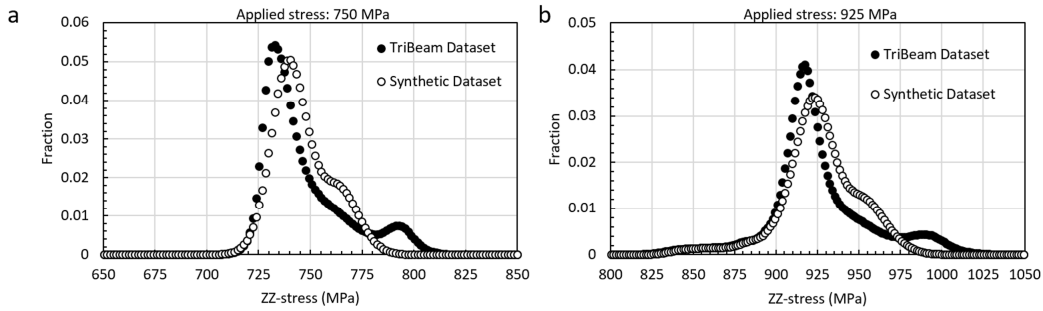


Figure 11 a. Distribution frequency of σ_{ZZ} for the 3D TriBeam data and the synthetic microstructure at an applied stress of a. 750 MPa and b. 925 MPa. The degrees of heterogeneities in the stress values are significantly increased by the presence of MTRs in the elastic and plastic regimes.

Further evidence of the increased stress heterogeneities in the 3D TriBeam dataset are in the distribution frequency of σ_{ZZ} , shown in figure 11, at applied stresses of 750 MPa and 925 MPa. 1.5 MPa bins are used for these plots. The 750 MPa and 925 MPa load steps were selected in order to show the deformation behavior in the elastic and early plasticity regimes. A significantly higher spread in σ_{ZZ} values is present in the experimentally collected microstructure at 750 MPa. Considering frequencies higher than 0.2 %, the values range from 716 MPa to 805 MPa for the TriBeam microstructure versus 716 MPa to 784 MPa for the synthetic microstructure. Two peaks are noticed for the experimentally collected dataset: 733 MPa and 793 MPa. In contrast, only one main peak at 740 MPa is observed for the synthetic dataset. An inflexion in the 930 MPa range indicates that a secondary overlapping peak might be present at stress values around 760 MPa. These observations unambiguously reveal a higher degree of stress heterogeneities in the experimental TriBeam microstructure in the elastic regime, with a very similar conclusion being drawn from the closely matching distributions in the early plasticity regime shown in figure 11b. However, an additional plateau is present for both microstructures in the domain ranging from 825 MPa to 890 MPa. A comparison of the spatial location of these voxels and the location of voxels associated with significant plastic strain indicates that these low magnitudes are plastically deforming grains. This is an evidence of load shedding from soft grains on to hard grains due to the heterogeneous plastic deformation. The previous analysis reveals an increased degree of stress heterogeneity which is promoted by the presence of MTRs in both the elastic and plastic regimes. In order to confirm the role of these heterogeneities on the early slip activity and the yield behavior, the crystallographic orientation of the participating grains is investigated.

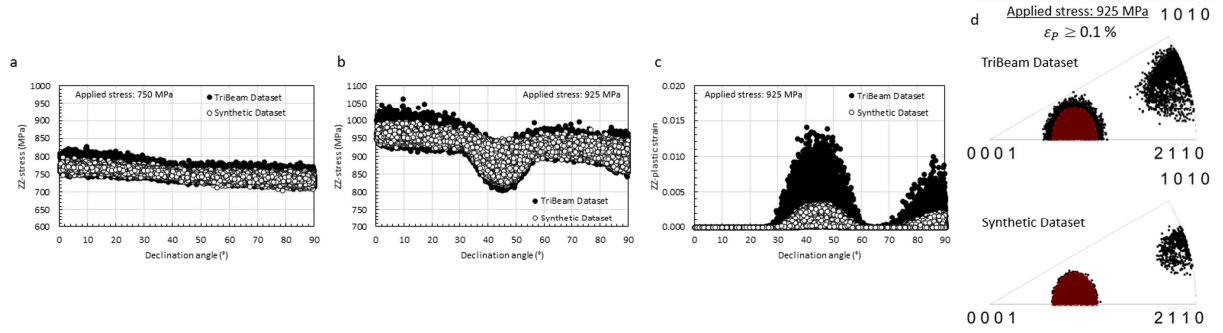


Figure 12 a. Grain averaged σ_{ZZ} plotted as a function of the declination angle for the experimentally collected and the synthetic microstructures at an applied stress of 750 MPa, b. grain averaged σ_{ZZ} plotted as a function of the declination angle for the 3D TriBeam and the synthetic microstructures at an applied stress of 925 MPa, c. Grain averaged $\epsilon_{p,ZZ}$ plotted as a function of the declination angle for the 3D TriBeam and the synthetic microstructures at an applied stress of 925 MPa and d. Crystallographic orientation relative to the loading axis of grains with an average magnitude of $\epsilon_{p,ZZ}$ higher than 10^{-3} are plotted on inverse pole figures. These plots reveal a higher degree of stress and plastic strain heterogeneities at a similar applied stress for the microstructure containing MTRs, and a larger orientation domain with slip activity in the experimentally collected microstructure.

Figure 12a. reports the magnitude of σ_{ZZ} averaged over each grain as a function of the declination angle (the angle between the c-axis of the hexagonal close packed lattice and the loading direction - see figure 4) at an applied stress about 750 MPa for the experimentally collected and synthetic microstructures. Qualitative observations of the average behavior reveal a similar evolution of the stress value with respect to the declination angle. The main noticeable feature is the increased spread in the values for a given declination angle. While they spread over a 50 MPa range for the synthetic microstructure, a spread over 75 MPa is observed for the 3D TriBeam microstructure. Similar to the deformation behavior of the experimentally collected microstructure in the elastic regime, the scatter in declination angle reflects the effect of the surrounding microstructure. Hence, the presence of MTRs favors stress heterogeneities for all grain orientations, including those with early slip activation.

A similar analysis was carried out at an applied stress of 925 MPa. The magnitude of σ_{ZZ} averaged over each grain is shown as a function of the declination angle in figure 12b. The magnitude of the scatter is higher for the 3D TriBeam microstructure than for the synthetic microstructure for any value of the declination angle, as observed in the elastic regime. Also, the evolution of the stress magnitude with respect to the declination angle differs significantly from the one in the elastic regime. A major drop in the stress values is observed for angles around 45° and a minor drop for angles around 90° . These angles correspond to the crystallographic orientations with basal and prismatic Schmid factors of 0.5. Slip activation and the resulting plastic strain induce a local stress relaxation that leads to the observed stress drop. This is confirmed by the plot of the magnitude of $\epsilon_{p,ZZ}$ averaged over each grain as a function of the declination angle shown in figure 12c. The stress drops, and their intensities, seem tightly related to the magnitude of the plastic strain. Two peaks are noticed: a major peak for a declination angle about 45° and a minor peak for a declination angle about 90° . Since the 45° peak is associated with basal slip and the 90° peak is associated with prismatic slip, then it reveals that a higher plastic strain is experienced by grains where basal slip operates, at least in the early stages of deformation. A similar feature was recently reported from experimental characterizations [30]. Regarding the effect of MTRs, the magnitudes of the peaks for the experimentally collected microstructure are higher than the magnitudes of the peaks for the synthetic microstructure. While the plastic strain in grains deforming by basal slip reaches 1.4×10^{-2} in the 3D TriBeam microstructure, the plastic strain remains below 4×10^{-3} for the synthetic microstructure. Grains deforming by prismatic slip reach 1×10^{-2} plastic strain in the 3D TriBeam microstructure versus 3×10^{-3} in the synthetic microstructure. Therefore, the presence of MTRs favors stress heterogeneities in the elastic regime, however also allow higher plastic strain magnitudes in the plastic regime.

Grains where slip is active were identified using a criterion based on an average plastic strain magnitude higher than 10^{-3} . The crystallographic orientations of these grains are plotted with respect to the

loading axis on an inverse pole figure in figure 12d. For both 3D datasets, two distinct orientation domains are associated with slip activity. Considering the Schmid factor iso-contours reported in [40], these regions match with orientation domains associated with high Schmid factors for basal and prismatic slip systems. This finding unambiguously confirms the previous analysis associating the 45° peaks with basal slip and the 90° peaks with prismatic slip. Another interesting feature is the size of these orientation domains, which depends on the degree of microtexture. The larger orientation domains associated with enhanced plastic strain are more frequent in the TriBeam microstructure than in the synthetic microstructure. Hence, the differences in plastic strain magnitudes previously noticed also depend on the size of the orientation domains associated with plastic deformation.

4 Discussion

The TriBeam tomography technique was employed to collect and reconstruct a sufficiently large volume of Ti-6Al-4V microstructural information containing several MTRs, while maintaining μm -scaled resolution to capture the α grain sizes, morphologies and orientations. These features are critical to properly reproduce the experimental behavior. The behavior in the early stages of deformation was simulated using a crystal plasticity framework. For comparison purposes, a tensile test was performed and 3D TriBeam data was collected from below the surface where surface strain measurements were made with SEM DIC in a previous study [6]. The comparison of simulated and experimental strain behaviors revealed a realistic reproduction of deformation at the grain and aggregate scales. This agreement may deteriorate at higher strains owing to the increasing importance of slip transfer, which is not properly accounted for in standard simulations of polycrystals [42]. Its contribution is not expected to be important for small strain, such as investigated in this work which mainly focuses on how elastic and plastic anisotropies influence the very onset of slip activity. However, a recent study suggested that a crystal plasticity formulation with dislocation densities as internal variables, which is slightly different from the one presently employed, seems to be able to capture both overall stress response and local plastic strain development [43].

The analysis of the stress and plastic strain fields in the TriBeam microstructure in the elastic and plastic regimes revealed heterogeneities in the local mechanical response with the presence of MTRs. In particular, MTRs with a dominant $[0001]$ orientation along the loading direction have an influence on the stress and plastic strain fields. Both stress and plastic strain concentrations are located in MTRs with a dominant $[0001]$ orientation. Early onset of slip activity was observed in the MTRs with a dominant $[0001]$ orientation [6,17]. This feature was assumed to stem from the elastic anisotropy of α titanium. [14,17], which is confirmed with the present simulations. High stress magnitudes are developed in MTRs with a dominant $[0001]$ orientation, which triggers local slip activity prior to slip outside the $[0001]$ MTRs. Importantly, the grains associated with the early slip activity do not possess a $[0001]$ orientation and also have a high Schmid factor for basal slip. This observation demonstrates that MTRs with a dominant $[0001]$ orientation cannot be considered as a single effective structural unit since properties of grains oriented with their c -axis aligned with the loading axis and oriented for an easy basal slip are both involved in the local deformation behavior.

The present observations are of critical importance for understanding fatigue properties and dwell-fatigue crack initiation, which are inherently associated with slip localization. Prior studies highlighted fatal fatigue crack initiation in α grains within MTRs with operating basal slip [13–16]. Based on comparisons between experiments and crystal plasticity simulations, the accumulated slip on the primary system seems critical for the initiation of transgranular microcracks [44,45]. The monotonic tension simulations performed in this study support the presence of strain hotspots located in MTRs with an overall dominant $[0001]$ orientation. Specific configurations composed of a soft grain, well-oriented for $\langle a \rangle$ slip, and a hard grain, poorly-oriented for $\langle a \rangle$ slip have been reported as critical microstructural arrangement for dwell-fatigue crack initiation [46,47]. The underlying process of crack initiation involves a large amount of plastic strain in the soft grain that induces load shedding into the hard grain where the high stress that cannot be

accommodated by $\langle a \rangle$ slip eventually leading to quasi-cleavage facet formation. Both of these requirements are met in the MTRs with a dominant $[0001]$ orientation, thus explaining the preferential occurrence of fatigue and dwell-fatigue crack initiation in these regions [13–16]. However, more than two grains might have to be considered to identify the fatal crack initiation site. The present simulations show that the 3D neighborhood has a significant effect on the presence of plastic strain hotspots. This is illustrated in figure 13 where two grains with similar orientations and different direct neighborhoods exhibit very different plastic strain levels. The highly strained grain seems surrounded by hard gains while no such grain is found around the grain with a lower plastic strain level. Further work is on-going to statistically analyze the influence of the direct neighborhood on the stress and strain hotspots.

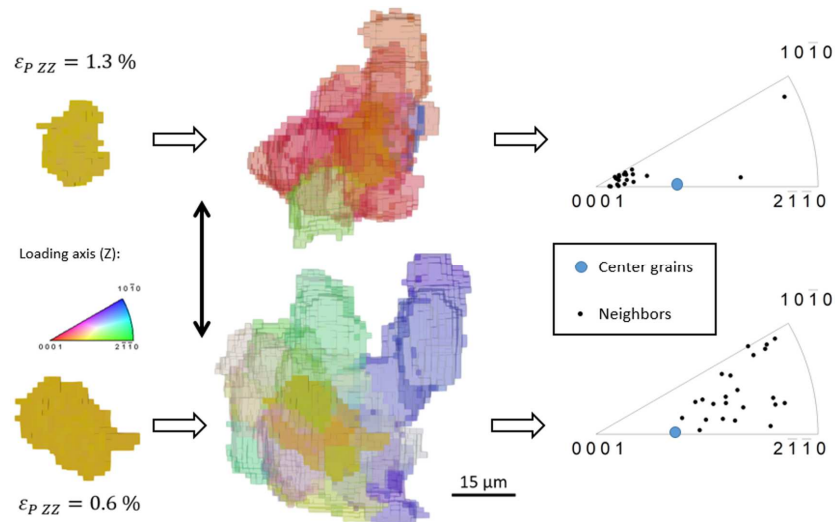


Figure 13 Two grains with similar orientations but highly different plastic strain levels (opaque colors) and their direct neighborhoods (transparent colors) are shown with colors indicating the crystallographic orientation relative to the loading direction. Crystallographic orientations relative to the loading direction are also plotted on inverse pole figures. They reveal that different strain levels are associated with neighbors exhibiting significantly different orientations.

Several researchers reported preferential crack initiation at the interface between “hard” and “soft” MTRs under cyclic loadings [48,49]. It is also interesting to notice that the long bands of strain localization and slip in the $[10\bar{1}0]$ MTRs in [6] initiate at the interface with a $[0001]$ MTR. The present simulations reveal that high stress values are observed in MTRs with a dominant $[10\bar{1}0]$ orientation near their interface with MTRs with a dominant $[0001]$ orientation. An early onset of slip activity is thus expected in these regions, which could be preferential locations for early crack nucleation. Both scenarios (i.e. crack initiation in MTRs or at the interface between MTRs) reveal that the location of crack initiation is highly influenced by stress and strain heterogeneities at the MTR scale. The competition between both types of locations is likely to depend on the size, shape and intensity of MTRs. More work is required in this direction for a more predictive understanding. However, while the main detrimental effect of MTRs is assigned to a minimal resistance to crack growth in such regions [11,12], the present results also suggest an early crack initiation induced by mechanical interactions due to their presence.

The complex mechanical behavior induced by the presence of MTRs was evidenced in this work through non-local mechanical effects. The mechanical state and behavior at a given point or in a given grain cannot be properly predicted based on the local properties or even those of its direct neighbors. Another striking aspect of the mechanical complexity of multi-scale microstructures is apparent in the comparison of the deformation behavior of microstructures with varying degrees of microtexture. In spite of the similar macrotexture, different deformation behaviors were observed for the experimentally collected and synthetic microstructures. Although the macroscopic elastic behavior was not significantly influenced by the degree of microtexture, the yield stress was decreased with MTRs, likely due to the heterogeneous character of the stress field. These heterogeneities, which impact all orientations, induce an early onset of slip activity as well as higher plastic strain magnitudes. Two major conclusions ensue from these results. The first regarding

simulation approaches; the spatial distribution of crystallographic orientations has to be considered in order to accurately simulate and reproduce the behavior of alloys and their microstructures. The present results demonstrate that a similar macrotexture is insufficient. Second, the tensile yield strength and fatigue properties of α/β titanium alloys could be improved through a careful control of processing conditions in order to reduce the degree of microtexture in industrial components. Although this idea is well established for dwell-fatigue, the present investigation demonstrates that the individual contributions of microtexture and macrotexture are important to a broader set of mechanical properties [50–52].

5 Conclusion

The present study reports numerical simulations on a 3D volume of Ti-6Al-4V microstructure containing more than 57000 α grains acquired by TriBeam tomography. The TriBeam captured both crystallographic orientations and grain morphologies over a large 3D volume of $198 \mu\text{m} \times 715.5 \mu\text{m} \times 508.5 \mu\text{m}$ that includes several MTRs. This is particularly important, as the mechanical response is sensitive to the grain morphologies and to the spatial distribution of orientations, as demonstrated in the present study. In order to unravel the effect of these MTRs on mechanical properties, a synthetic microstructure with a similar macrotexture but a different degree of microtexture was designed. Numerical simulation of the deformation behavior in the elastic and early stages of plastic deformation using crystal plasticity simulations based on fast-Fourier transforms provided the following findings:

- Examination of experimentally captured and simulated slip activities revealed a proper prediction of incipient slip locations at the MTR and grain scales, which demonstrates a realistic simulation of the onset of plastic deformation.
- MTRs with a dominant $[0001]$ orientation form both stress and plastic strain hotspots that play a critical role in the fatigue and dwell fatigue behavior of these materials.
- Early slip activity occurs within $[0001]$ microtextured regions in locally misoriented α grains that have a high Schmid factor for basal slip.
- High stresses are found in MTRs with a dominant $[0001]$ orientation but also in MTRs with a dominant $[10\bar{1}0]$ orientation, near their interface with MTRs with a dominant $[0001]$ orientation. This observation provides a mechanistic explanation for the initiation of cracks at the interface between such MTRs.
- In spite of a similar global texture, the degree of microtexture has a significant effect on the tensile behavior, and in particular on the yield strength. This result is explained by the MTR-induced heterogeneity of the stress field in the elastic regime, which favors an early onset of plastic slip, and then leads to higher plastic strain magnitudes for microstructures containing MTRs.
- The above-mentioned effects stem from complex mechanical interactions at different length-scales induced by the elastic and plastic anisotropies of α titanium. In particular, it reveals that the spatial distribution of crystallographic orientations has to be considered in order to accurately simulate and reproduce the behavior of alloys and their microstructures.

6 Acknowledgements

Computations were performed on the supercomputer facilities at the m eso-centre de calcul SPIN hosted by Poitiers University. JW, MPE, JCS and TMP gratefully acknowledge the support of ONR Grant N00014-19-2129.

7 References

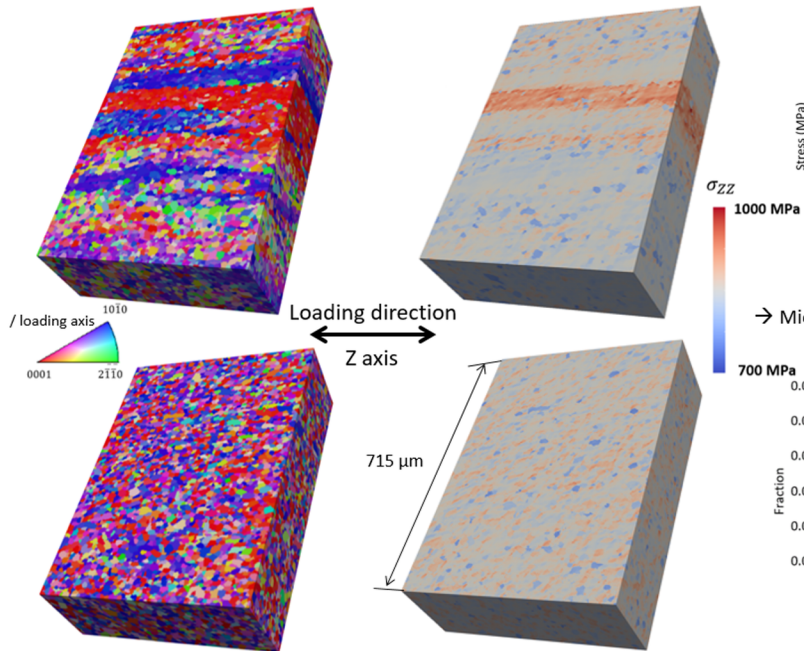
- [1] G. L utjering, J.C. Williams, Titanium, 2nd edition, Springer, Berlin; New York, 2007.

- [2] G. Lütjering, Influence of processing on microstructure and mechanical properties of (α + β) titanium alloys, *Mater. Sci. Eng. A-Struct.* 243 (1998) 32–45. doi:10.1016/S0921-5093(97)00778-8.
- [3] P. Castany, F. Pettinari-Sturmel, J. Douin, A. Coujou, In situ transmission electron microscopy deformation of the titanium alloy Ti–6Al–4V: Interface behaviour, *Mater. Sci. Eng. A-Struct.* 483–484 (2008) 719–722. doi:10.1016/j.msea.2006.10.183.
- [4] L. Germain, N. Gey, M. Humbert, P. Vo, M. Jahazi, P. Bocher, Texture heterogeneities induced by subtransus processing of near α titanium alloys, *Acta Mater.* 56 (2008) 4298–4308. doi:10.1016/j.actamat.2008.04.065.
- [5] A.L. Pilchak, J. Shank, J.C. Tucker, S. Srivatsa, P.N. Fagin, S.L. Semiatin, A dataset for the development, verification, and validation of microstructure-sensitive process models for near-alpha titanium alloys, *Integr. Mater. Manuf. Innov.* 5 (2016) 14. doi:10.1186/s40192-016-0056-1.
- [6] M.P. Echlin, J.C. Stinville, V.M. Miller, W.C. Lenthe, T.M. Pollock, Incipient slip and long range plastic strain localization in microtextured Ti-6Al-4V titanium, *Acta Mater.* 114 (2016) 164–175. doi:10.1016/j.actamat.2016.04.057.
- [7] M. Kasemer, M.P. Echlin, J.C. Stinville, T.M. Pollock, P. Dawson, On slip initiation in equiaxed α/β Ti-6Al-4V, *Acta Mater.* 136 (2017) 288–302. doi:10.1016/j.actamat.2017.06.059.
- [8] S. Hémerly, P. Nizou, P. Villechaise, In situ SEM investigation of slip transfer in Ti-6Al-4V: Effect of applied stress, *Mater. Sci. Eng. A-Struct.* 709 (2018) 277–284. doi:10.1016/j.msea.2017.10.058.
- [9] A.L. Pilchak, Fatigue crack growth rates in alpha titanium: Faceted vs. striation growth, *Scripta Mater.* 68 (2013) 277–280. doi:10.1016/j.scriptamat.2012.10.041.
- [10] A.L. Pilchak, A simple model to account for the role of microtexture on fatigue and dwell fatigue lifetimes of titanium alloys, *Scripta Mater.* 74 (2014) 68–71. doi:10.1016/j.scriptamat.2013.10.024.
- [11] V. Sinha, M.J. Mills, J.C. Williams, J.E. Spowart, Observations on the faceted initiation site in the dwell-fatigue tested ti-6242 alloy: Crystallographic orientation and size effects, *Metall. Mater. Trans. A.* 37 (2006) 1507–1518. doi:10.1007/s11661-006-0095-x.
- [12] V. Sinha, A.L. Pilchak, S.K. Jha, W.J. Porter, R. John, J.M. Larsen, Correlating Scatter in Fatigue Life with Fracture Mechanisms in Forged Ti-6242Si Alloy, *Metall. Mater. Trans. A.* 49 (2018) 1061–1078. doi:10.1007/s11661-017-4437-7.
- [13] K. Le Biavant, S. Pommier, C. Prioul, Local texture and fatigue crack initiation in a Ti-6Al-4V titanium alloy, *Fat. Fract. Eng. Mater. Struct.* 25 (2002) 527–545. doi:10.1046/j.1460-2695.2002.00480.x.
- [14] F. Bridier, P. Villechaise, J. Mendez, Slip and fatigue crack formation processes in an α/β titanium alloy in relation to crystallographic texture on different scales, *Acta Mater.* 56 (2008) 3951–3962. doi:10.1016/j.actamat.2008.04.036.
- [15] I. Bantounas, D. Dye, T.C. Lindley, The effect of grain orientation on fracture morphology during high-cycle fatigue of Ti–6Al–4V, *Acta Mater.* 57 (2009) 3584–3595. doi:10.1016/j.actamat.2009.04.018.
- [16] E. Uta, N. Gey, P. Bocher, M. Humbert, J. Gilgert, Texture heterogeneities in $\alpha\text{p}/\alpha\text{s}$ titanium forging analysed by EBSD-Relation to fatigue crack propagation, *J. Microsc.* 233 (2009) 451–459. doi:10.1111/j.1365-2818.2009.03141.x.
- [17] S. Hémerly, V.T. Dang, L. Signor, P. Villechaise, Influence of Microtexture on Early Plastic Slip Activity in Ti-6Al-4V Polycrystals, *Metall. Mater. Trans. A.* (2018) 1–9. doi:10.1007/s11661-018-4569-4.
- [18] S. Hémerly, A. Nait-Ali, M. Guéguen, P. Villechaise, Mechanical study of crystalline orientation distribution in Ti-6Al-4V: An assessment of micro-texture induced load partitioning, *Mater. Design.* 137 (2018) 22–32. doi:10.1016/j.matdes.2017.10.011.
- [19] A. Zeghadi, F. N’guyen, S. Forest, A.-F. Gourgues, O. Bouaziz, Ensemble averaging stress–strain fields in polycrystalline aggregates with a constrained surface microstructure – Part 1: anisotropic elastic behaviour, *Phil. Mag.* (2010). doi:10.1080/14786430601009509.
- [20] M.D. Uchic, M.A. Groeber, A.D. Rollett, Automated serial sectioning methods for rapid collection of 3-D microstructure data, *JOM-J. Min. Met. Mat. S.* 63 (2011) 25–29. doi:10.1007/s11837-011-0041-2.
- [21] T.L. Burnett, R. Kelley, B. Winiarski, L. Contreras, M. Daly, A. Gholinia, M.G. Burke, P.J. Withers, Large volume serial section tomography by Xe Plasma FIB dual beam microscopy, *Ultramicroscopy.* 161 (2016) 119–129. doi:10.1016/j.ultramic.2015.11.001.
- [22] H.F. Poulsen, S.F. Nielsen, E.M. Lauridsen, S. Schmidt, R.M. Suter, U. Lienert, L. Margulies, T. Lorentzen, D. Juul Jensen, Three-dimensional maps of grain boundaries and the stress state of

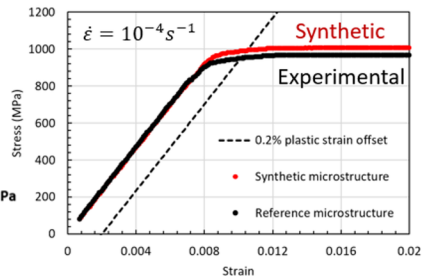
- individual grains in polycrystals and powders, *J. Appl. Crystallogr.* 34 (2001) 751–756. doi:10.1107/S0021889801014273.
- [23] M.P. Echlin, M. Straw, S. Randolph, J. Filevich, T.M. Pollock, The TriBeam system: Femtosecond laser ablation in situ SEM, *Materials Characterization*. 100 (2015) 1–12. doi:10.1016/j.matchar.2014.10.023.
- [24] F.P.E. Dunne, D. Rugg, A. Walker, Lengthscale-dependent, elastically anisotropic, physically-based hcp crystal plasticity: Application to cold-dwell fatigue in Ti alloys, *Int. J. Plasticity*. 23 (2007) 1061–1083. doi:10.1016/j.ijplas.2006.10.013.
- [25] V. Hasija, S. Ghosh, M.J. Mills, D.S. Joseph, Deformation and creep modeling in polycrystalline Ti–6Al alloys, *Acta Mater.* 51 (2003) 4533–4549. doi:10.1016/S1359-6454(03)00289-1.
- [26] J.R. Mayeur, D.L. McDowell, A three-dimensional crystal plasticity model for duplex Ti–6Al–4V, *Int. J. Plasticity*. 23 (2007) 1457–1485. doi:10.1016/j.ijplas.2006.11.006.
- [27] M. Hamid Pourian, P. Pilvin, F. Bridier, P. Bocher, Modeling the elastoplastic behaviors of alpha Ti-alloys microstructure using Cellular Automaton and finite element methods, *Comp. Mater. Sci.* 99 (2015) 33–42. doi:10.1016/j.commatsci.2014.11.027.
- [28] R.A. Lebensohn, A.K. Kanjarla, P. Eisenlohr, An elasto-viscoplastic formulation based on fast Fourier transforms for the prediction of micromechanical fields in polycrystalline materials, *Int. J. Plasticity*. 32–33 (2012) 59–69. doi:10.1016/j.ijplas.2011.12.005.
- [29] H. Moulinec, P. Suquet, A numerical method for computing the overall response of nonlinear composites with complex microstructure, *Comput. Method. Appl. M.* 157 (1998) 69–94. doi:10.1016/S0045-7825(97)00218-1.
- [30] M.A. Groeber, M.A. Jackson, DREAM.3D: A Digital Representation Environment for the Analysis of Microstructure in 3D, *Integrating Mater.* 3 (2014) 5. doi:10.1186/2193-9772-3-5.
- [31] S. Hémerly, P. Villechaise, In situ EBSD investigation of deformation processes and strain partitioning in bi-modal Ti-6Al-4V using lattice rotations, *Acta Mater.* 171 (2019) 261–274. doi:10.1016/j.actamat.2019.04.033.
- [32] <https://sourcesup.renater.fr/foxtrot/html/>
- [33] T. Neeraj, D.-H. Hou, G.S. Daehn, M.J. Mills, Phenomenological and microstructural analysis of room temperature creep in titanium alloys, *Acta Materialia*. 48 (2000) 1225–1238. doi:10.1016/S1359-6454(99)00426-7.
- [34] E.S. Fisher, C.J. Renken, Single-Crystal Elastic Moduli and the hcp bcc Transformation in Ti, Zr, and Hf, *Phys. Rev.* 135 (1964) A482–A494. doi:10.1103/PhysRev.135.A482.
- [35] R.A. Adebisi, S. Sathish, A.L. Pilchak, P.A. Shade, Elastic constants of α Ti-7Al measured using resonant ultrasound spectroscopy, *AIP Conf. Proc.* 1706 (2016) 070005. doi:10.1063/1.4940523.
- [36] S. Hémerly, A. Nait-Ali, P. Villechaise, Combination of in-situ SEM tensile test and FFT-based crystal elasticity simulations of Ti-6Al-4V for an improved description of the onset of plastic slip, *Mech. Mater.* (n.d.). doi:10.1016/j.mechmat.2017.03.013.
- [37] S. Hémerly, P. Villechaise, Investigation of Size Effects in Slip Strength of Titanium Alloys: α Nodule Size Dependence of the Critical Resolved Shear Stress, *Metall. Mater. Trans. A.* (2018) 1–4. doi:10.1007/s11661-018-4678-0.
- [38] D.C. Pagan, P.A. Shade, N.R. Barton, J.-S. Park, P. Kenesei, D.B. Menasche, J.V. Bernier, Modeling slip system strength evolution in Ti-7Al informed by in-situ grain stress measurements, *Acta Mater.* 128 (2017) 406–417. doi:10.1016/j.actamat.2017.02.042.
- [39] D. Deka, D.S. Joseph, S. Ghosh, M.J. Mills, Crystal plasticity modeling of deformation and creep in polycrystalline Ti-6242, *Metall. Mater. Trans. A* 37 (2006) 1371–1388. doi:10.1007/s11661-006-0082-2.
- [40] F. Bridier, P. Villechaise, J. Mendez, Analysis of the different slip systems activated by tension in a α/β titanium alloy in relation with local crystallographic orientation, *Acta Mater.* 53 (2005) 555–567. doi:10.1016/j.actamat.2004.09.040.
- [41] S. Hémerly, P. Villechaise, On the influence of ageing on the onset of plastic slip in Ti-6Al-4V at room temperature: Insight on dwell fatigue behavior, *Scripta Mater.* 130 (2017) 157–160. doi:10.1016/j.scriptamat.2016.11.042.
- [42] T.R. Bieler, R. Alizadeh, M. Peña-Ortega, J. Llorca, An analysis of (the lack of) slip transfer between near-cube oriented grains in pure Al, *Int. J. Plasticity* 118 (2019) 269–290. doi:10.1016/j.ijplas.2019.02.014.

- [43] Z. Zheng, S. Waheed, D.S. Balint, F.P.E. Dunne, Slip transfer across phase boundaries in dual phase titanium alloys and the effect on strain rate sensitivity, *Int. J. Plasticity* 104 (2018) 23–38. doi:10.1016/j.ijplas.2018.01.011.
- [44] A. Manonukul, F.P.E. Dunne, High- and low-cycle fatigue crack initiation using polycrystal plasticity, *P. R. Soc. A.* 460 (2004) 1881–1903. doi:10.1098/rspa.2003.1258.
- [45] L. Signor, P. Villechaise, T. Ghidossi, E. Lacoste, M. Gueguen, S. Courtin, Influence of local crystallographic configuration on microcrack initiation in fatigued 316LN stainless steel: Experiments and crystal plasticity finite elements simulations, *Mater. Sci. Eng. A-Struct.* 649 (2016) 239–249. doi:10.1016/j.msea.2015.09.119.
- [46] W.J. Evans, M.R. Bache, Dwell-sensitive fatigue under biaxial loads in the near-alpha titanium alloy IMI685, *Int. J. Fatigue.* 16 (1994) 443–452. doi:10.1016/0142-1123(94)90194-5.
- [47] F.P.E. Dunne, A. Walker, D. Rugg, A systematic study of hcp crystal orientation and morphology effects in polycrystal deformation and fatigue, *P. R. Soc. A.* 463 (2007) 1467–1489. doi:10.1098/rspa.2007.1833.
- [48] K. Zhang, K.V. Yang, A. Huang, X. Wu, C.H.J. Davies, Fatigue crack initiation in as forged Ti–6Al–4V bars with macrozones present, *Int. J. Fatigue* 80 (2015) 288–297. doi:10.1016/j.ijfatigue.2015.05.020.
- [49] P.O. Tympel, T.C. Lindley, E.A. Saunders, M. Dixon, D. Dye, Macrozones and dwell fatigue crack initiation in Ti-6Al-4V, in: V. Venkatesh, A.L. Pilchak, J.E. Allison, S. Ankem, R. Boyer, J. Christodoulou, H.L. Fraser, M.A. Imam, Y. Kosaka, H.J. Rack, A. Chatterjee, A. Woodfield (Eds.), *Proceedings of the 13th World Conference on Titanium*, John Wiley & Sons, Inc., 2016: pp. 985–991. doi:10.1002/9781119296126.ch168.
- [50] D. Lunt, J.Q. da Fonseca, D. Rugg, M. Preuss, Microscopic strain localisation in Ti-6Al-4V during uniaxial tensile loading, *Mater. Sci. Eng. A-Struct.* 680 (2017) 444–453. doi:10.1016/j.msea.2016.10.099.
- [51] M.R. Bache, W.J. Evans, Impact of texture on mechanical properties in an advanced titanium alloy, *Mater. Sci. Eng. A-Struct.* 319–321 (2001) 409–414. doi:10.1016/S0921-5093(00)02034-7.
- [52] M.R. Bache, W.J. Evans, V. Randle, R.J. Wilson, Characterization of mechanical anisotropy in titanium alloys, *Mater. Sci. Eng. A-Struct.* 257 (1998) 139–144. doi:10.1016/S0921-5093(98)00832-6.

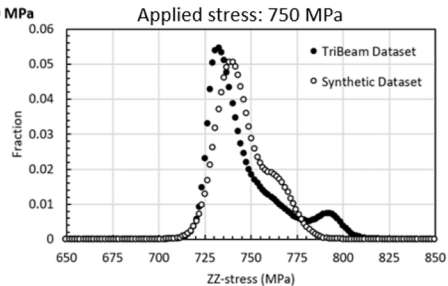
Experimentally collected microstructure



Synthetic microstructure with similar macrotexture



→ Microtextured regions induce a lower yield strength



→ Microtextured regions induce stress heterogeneities